ACS Sustainable Chemistry & Engineering

Research Article

pubs.acs.org/journal/ascecg

Microwave-Assisted Nonaqueous Sol–Gel Synthesis: From Al:ZnO Nanoparticles to Transparent Conducting Films

Li Luo,[†] Marta D. Rossell,[†,∥] Dan Xie,[‡,⊥] Rolf Erni,[§] and Markus Niederberger*[,†]

[†]Laboratory of Multifunctional Materials, Department of Materials, ETH Zurich, Wolfgang-Pauli-Strasse 10, 8093 Zurich, Switzerland

[‡]Laboratory of Crystallography, Department of Materials, ETH Zurich, Wolfgang-Pauli-Strasse 10, 8093 Zurich, Switzerland

[§]Electron Microscopy Center, EMPA, Swiss Federal Laboratories for Materials Science and Technology, Überlandstrasse 129, 8600 Dübendorf, Switzerland

Supporting Information

ABSTRACT: Al:ZnO nanoparticles with different doping levels were synthesized by a microwave-assisted nonaqueous sol–gel route in benzyl alcohol and subsequently processed into transparent conducting films. The crystal structure, crystal size and shape, and doping level of the nanoparticles were analyzed in detail by Rietveld refinement from powder X-ray diffraction (PXRD) data and transmission electron microscopy (TEM). Study of the thermal stability gave evidence that the material did not phase-separate up to 600 °C. Films were prepared on fused silica substrates by dip-coating from Al:ZnO nanoparticle dispersions, followed by a microwave-assisted densification step. According to scanning electron microscopy (SEM) and atomic force microscopy (AFM) measurements, the films were homogeneous over large areas with a root-mean-square (Rms) roughness of about 10 nm. A minimum resistivity of 2.35×10^{-2} Ω·cm was achieved for a 357-nm-thick Al:ZnO film with an initial Al-to-Zn mol ratio of 1:9 after postannealing under N_2. The changes of the electrical properties of the films could be well-explained on the basis of varying initial doping levels and crystal sizes of the nanoparticle building blocks. The average transmittance of the films in the visible light range was higher than 90%, and especially for green light it reached up to 95%.

KEYWORDS: *Microwave-assisted synthesis, Al-doped ZnO nanoparticles, Transparent conducting films*

INTRODUCTION

Transparent conducting oxide (TCO) films with a large energy band gap exhibit high electrical conductivity and high optical transmittance in the visible region. These unique properties make them suitable for a variety of applications such as chlorine, ozone, and methane gas sensors;[1−3] flat panel, e-paper, and touch-panel displays;[4,5] light-emitting diodes;[6−10] smart windows;[11−13] and solar cells.[14−16]

Transparent conducting films of In_2O_3, SnO_2, CdO, and ZnO have been known for decades. Currently, $Sn:In_2O_3$ (ITO) is well-established on an industrial scale due to the best electrical conductivity among these oxides. However, the price of indium is increasing due to the rapidly growing demand for ITO. As a promising alternative to ITO, Al:ZnO has moved into the focus because of its lower cost, large band gap, thermal stability, and abundance in nature.[17]

Because the electrical and optical properties of TCO films depend markedly on the microstructure, stoichiometry, and nature of the impurities present, the deposition technique plays an important role. Various techniques for the growth of TCO films, such as chemical vapor deposition (CVD), pulsed laser deposition (PLD), sputtering, thermal evaporation, and liquid-phase deposition, have been investigated intensively. Some reported electrical and optical properties of Al:ZnO films deposited by different techniques are summarized in Table 1. Each technique has its own strengths and weaknesses. Until now, most industrially applied techniques that produce high-quality films are vapor-phase deposition methods. However, they are expensive because of the high vacuum needed during the deposition of the films and the frequently required cleaning procedure of the deposition chambers. Moreover, these methods have approached the technological limit and are therefore difficult to be optimized further. For all these reasons, great efforts have been made to find alternative techniques, among which liquid-phase deposition routes are particularly promising from an energy, as well as from a cost-saving, point of view. However, the quality of such wet chemically produced films is not yet good enough to be used as TCOs in technological applications.

Within this work, a versatile film-deposition process using a combination of the microwave-assisted nonaqueous sol–gel process[24−26] with dip-coating was developed. The procedure itself is quite straightforward. First, Al:ZnO nanoparticles with varying Al concentrations were synthesized by the microwave

Received: July 30, 2012
Revised: September 15, 2012
Published: November 2, 2012

   dx.doi.org/10.1021/sc300073d | ACS Sustainable Chem. Eng. 2013, 1, 152−160

Table 1. Properties of Al:ZnO Films Deposited by Different Techniques

deposition technique	resistivity (Ω·cm)	transmittance (%)	thickness (nm)	remarks	ref.
Vapor phase					
sputtering	5.0×10^{-4}	85	300	O_2/Ar	18
PLD	4.5×10^{-4}	87	730		19
CVD	3.0×10^{-4}	85	750		20
Liquid phase					
spray pyrolysis	3.6×10^{-2}	83	330		21
	3.0×10^{-3}	74	3200		21
sol–gel	$>1.0 \times 10^{2}$	98	2000	annealing in air	22
	10	96	2000	annealing in vacuum	22
	3.2×10^{-2}	93	2000	annealing in H_2/N_2	22
	4.0×10^{-3}	93	2000	infiltration twice	22
nanoparticle dispersion	2.6×10^{-1}	77	812	annealing in H_2/N_2	23

method, and then films were dip-coated on substrates from these nanoparticle dispersions. The main advantages of this process are (i) phase-pure nanoparticles with high crystallinity and narrow particle size distributions can be obtained in just a few minutes; (ii) the composition of the material can be well-controlled; (iii) multicomponent films can be achieved easily;[27] (iv) there is almost no waste of raw material; and (v) the equipment needed is simple. The main disadvantage of the method is that a high-temperature annealing step is unavoidable.[28]

EXPERIMENTAL SECTION

Materials. Zn(II) acetate (99.99%), Al(III) isopropoxide (99.99+ %), and benzyl alcohol (99.8%, anhydrous) were purchased from Aldrich. All chemicals were used as-received without further purification.

Synthesis of Al:ZnO Nanoparticles. Al:ZnO nanoparticles were synthesized using a microwave-assisted nonaqueous sol–gel method. In a glovebox with Ar atmosphere, Al(III) isopropoxide was added to a 10 mL vessel according to the desired doping level (Al/(Al + Zn) from 0 to 30 mol %). Then, Zn(II) acetate was added to reach 1 mmol of total precursors. The error of initial weighing was ±0.2 mg. Afterward, 5 mL of benzyl alcohol was added, and the vessel was sealed with a Teflon cap and taken out of the glovebox. The reaction mixture was heated by a microwave reactor (CEM Discover) at 180 °C for 3 min with high stirring rate. The precipitate was separated from the liquid phase by centrifugation and washed once with ethanol. One part of the precipitate was dried at 60 °C for characterization of the nanoparticles, whereas the other part was kept in wet form and then dispersed in absolute ethanol (without any surfactants) for film preparation; the solid concentration of the dispersion is about 10 mg/mL.

Film Preparation. A film was prepared on a fused silica substrate cleaned by ethanol using repeated dip-coating from the dispersion under ambient atmosphere using a NIMA dip-coater. The down speed was set at 60 mm/min, and the withdrawal speed was 5 mm/min. After each dip the films were heat-treated in air at 300 °C for 10 min in a preheated furnace. After depositing 6–12 layers, the substrates with the films were immersed into the precursor solution, and the microwave-assisted reaction was repeated in the presence of the films. This densification step could be repeated 1–3 times. Afterward, the so-densified films were annealed in air at 600 °C for 2 h, followed by naturally cooling down to room temperature. The ramping temperature was set to 3 °C/min. To investigate the influence of annealing atmosphere, some of the films were annealed in nitrogen at 600 °C for another 1 h.

Characterization. The powder X-ray diffraction (PXRD) patterns were measured in Bragg–Brentano mode and in θ–2θ geometry with Cu Kα radiation on a Philips diffractometer PW1800 equipped with a secondary monochromator. The high-temperature XRD (HTXRD) patterns were measured in Bragg–Brentano mode and in θ–2θ geometry with Cu Kα radiation on a PANalytical X'Pert Pro equipped with a high-temperature chamber (HTK 1200, Anton Paar). The Rietveld refinement was performed using the program *TOPAS*-Academic V4.1.[29] The peak shape function used to fit the patterns is the modified Thompson–Cox–Hastings pseudo-Voigt function.[30] Peak asymmetry due to axial divergence was calculated by the model proposed by Finger et al.[31] Linear absorption coefficient was used for adjusting the peak shape due to sample transparency. The preferred orientation correction was performed based on the March–Dollase model.[32] The Double–Voigt approach was used to model the microstructure (size and strain) effects and calculate the volume-weighted domain size (D_V).[33] A potential source of error in Bragg–Brentano geometry is that of surface roughness;[34] therefore, correction suggested by Pitschke et al. was applied during the refinement.[35]

Transmission electron microscopy (TEM), high-resolution transmission electron microscopy (HRTEM), energy-filtered transmission electron microscopy (EFTEM), and energy dispersive X-ray spectroscopy (EDX) investigations were performed on a JEOL 2200FS TEM/STEM operated at 200 kV and equipped with an in-column Omega-type energy filter. EFTEM was used to analyze the elemental distribution of Al, Zn, and O. The conventional three-window technique was used to obtain element-specific images. The final dopant concentration was analyzed by EDX. The microstructure and thickness of the films were characterized using scanning electron microscopy (SEM, Carl Zeiss LEO 1530) equipped with a field-emission gun operated at 5 kV. The surfaces of the films were sputter-coated with a platinum layer to reduce any charge effect. The element maps of moisture surface were obtained using a FEI Nova NanoSEM 230 equipped with an Oxford X-MAX EDX detector. The surface roughness of the films was characterized by atomic force microscopy (AFM, Agilent 5500) using intermittent contact mode.

The infrared spectra of the powders were recorded in a wavenumber range of 375–4000 using a Bruker ALPHA FT-IR (Fourier transformer infrared) spectrophotometer. The UV–vis reflection spectra of the powders were measured on a JASCO V-670 spectrophotometer with ILN-725 integrating sphere, while the transmission spectra of the films were measured with standard mode. The band gaps of the samples were determined from the reflectance of the powder, which has been proven to be a standard technique.[36−38]

The electrical properties of the films were measured at room temperature using the Van der Pauw method on a Hall Effect measurement system (Ecopia HMS-3000) with a 0.55 T magnet kit. The film was cut into a squared piece with a size of 5 × 5 mm and contacted to the measurement template with metallic indium.

RESULTS AND DISCUSSION

Al-Doped ZnO Nanoparticles. *Structure, Morphology, and Composition.* Figure 1 shows the PXRD patterns of $Al_nZn_{1-n}O$ with the initial dopant concentration of n = 0, 0.02, 0.05, 0.10, 0.15, 0.20, and 0.30. All samples maintained the wurtzite *hcp* structure of ZnO without detectable impurities.

dx.doi.org/10.1021/sc300073d | ACS Sustainable Chem. Eng. 2013, 1, 152–160

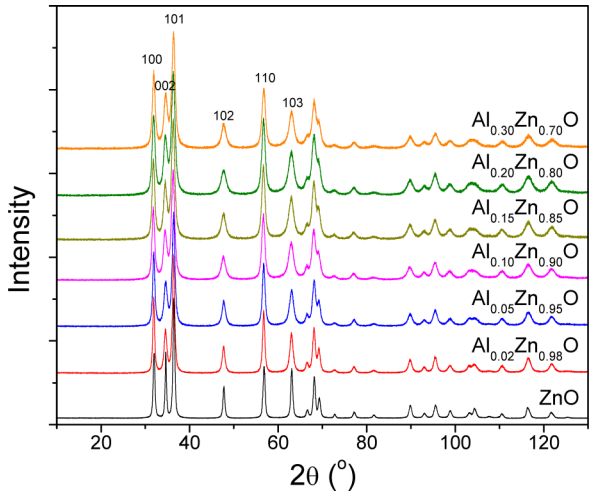

Figure 1. PXRD patterns of $Al_nZn_{1-n}O$ with the initial dopant concentration of n = 0, 0.02, 0.05, 0.10, 0.15, 0.20, and 0.30.

The PXRD patterns exhibit an increase of the full width at half-maximum (fwhm) of the diffraction peaks with increasing Al concentration, pointing to a decrease of the crystallite size upon incorporation of the dopant and/or an increase of the microstrain.

The PXRD patterns for the Al:ZnO compounds with different initial Al concentrations were analyzed by the Rietveld method. The phase content, lattice parameters, volume-weighted domain size (D_V), preferred orientation effect, and doping level (atomic site occupancy) for each material were investigated in detail, and the results are summarized in Table 2.

For the undoped ZnO nanoparticles, the lattice parameters are a = 3.249 Å and c = 5.206 Å, agreeing well with the reported values of 3.249 and 5.205 Å (ICDD PDF no. 36-1451). The lattice parameters a and c of Al:ZnO versus different initial Al concentrations were plotted in Figure 2. Both a and c decrease with increasing Al concentration up to 20 mol % but slightly increase with further increase of the Al concentration to 30 mol %. The variation of c is much more significant than that of a. The decrease of the lattice parameters is due to the fact that the ionic radius of Al^{3+} (0.54 Å) is smaller than that of Zn^{2+} (0.74 Å).[39] The more Al atoms are incorporated into the lattice, the smaller is the unit cell. Refinement of the atomic occupancy revealed that the doping level saturated around 8 at. %. Figure 3 shows the doping level determined by Rietveld refinement and EDX versus the initial Al concentration. The doping level increases from 0 to 10 mol % of Al. At 10 mol % it approached the saturation range, and thereafter only slightly increased

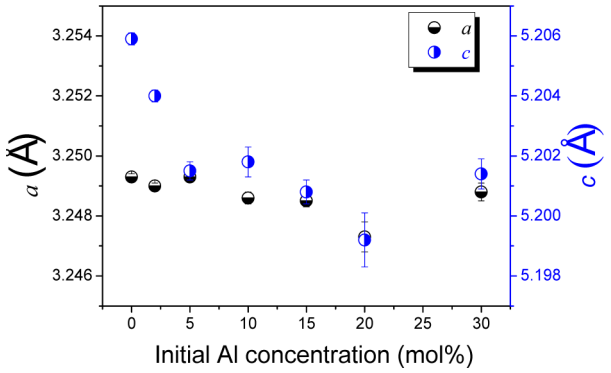

Figure 2. Lattice parameters of Al:ZnO nanocrystals with different initial Al concentrations.

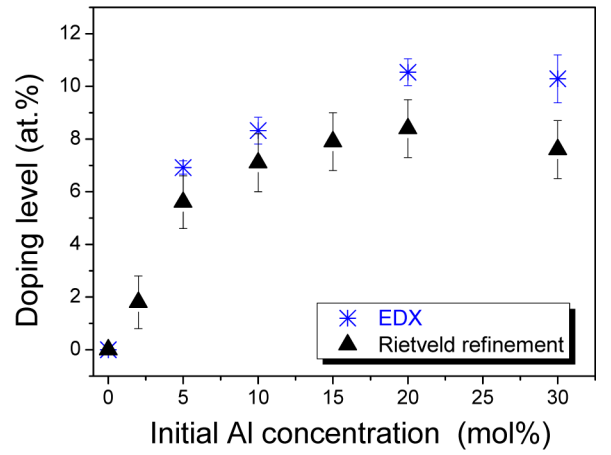

Figure 3. Doping level determined by Rietveld refinement and EDX.

further from 10 to 30 mol %. Whereas at doping levels ≤5 mol % the initially targeted and finally achieved doping levels agreed very well, at higher doping levels the discrepancy became larger. Obviously, the dopant is not quantitatively incorporated into the ZnO, which means that at higher concentrations a major part of the aluminum isopropoxide remained unreacted and was washed away during the recovery of the precipitate. Figure 4 shows the dependence of the crystal size (volume-weighted domain size, D_V) of the Al:ZnO nanoparticles on different initial Al concentrations. The crystal size reduced from about 18 to 13 nm after 2 mol % doping, and it further reduced slightly to ca. 9 nm by increasing the doping level. It has been proven before that the surface energy and the crystal growth are dependent on the dopant and its concentration.[40]

Table 2. Calculated Lattice Parameters, D_V, Doping Level, and Rietveld Agreement Factors of the $Al_nZn_{1-n}O$ (n = 0, 0.02, 0.05, 0.10, 0.15, 0.20, and 0.30) Compounds

	Rietveld refinement						
sample	a [Å]	c [Å]	V [Å^3]	Rwp	χ^2	D_V [nm]	doping level
ZnO	3.2493(1)	5.2059(2)	47.599(4)	6.657	1.474	18.2(3)	
$Al_{0.02}Zn_{0.98}O$	3.2490(1)	5.2040(2)	47.574(4)	9.291	1.600	13.0(3)	0.018(10)
$Al_{0.05}Zn_{0.95}O$	3.2493(1)	5.2015(3)	47.558(4)	9.703	1.706	11.5(4)	0.056(10)
$Al_{0.10}Zn_{0.90}O$	3.2486(2)	5.2018(5)	47.543(8)	10.130	1.879	13.1(17)	0.071(11)
$Al_{0.15}Zn_{0.85}O$	3.2485(2)	5.2008(4)	47.528(6)	10.107	1.786	12.9(16)	0.079(11)
$Al_{0.20}Zn_{0.80}O$	3.2473(5)	5.1992(9)	47.479(17)	9.829	1.878	10.9(22)	0.084(11)
$Al_{0.30}Zn_{0.70}O$	3.2488(3)	5.2014(5)	47.546(10)	9.106	1.485	9.3(3)	0.076(11)

dx.doi.org/10.1021/sc300073d | ACS Sustainable Chem. Eng. 2013, 1, 152−160

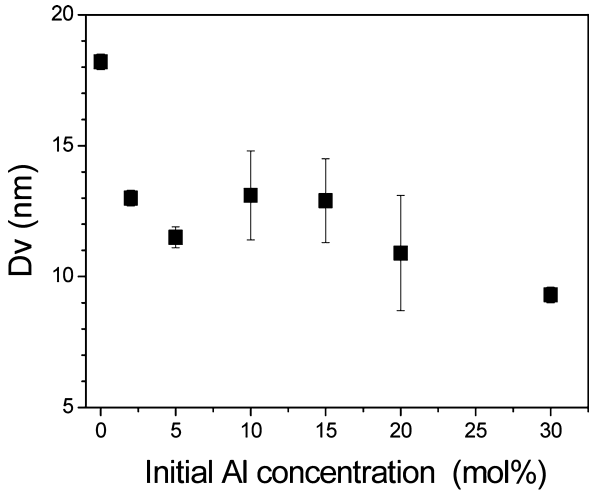

Figure 4. Dependence of the crystal size of Al:ZnO on the initial Al concentration.

Figure 5a displays a TEM image of $Al_{0.20}Zn_{0.80}O$ nanoparticles. The morphology of these nanoparticles is mainly roundish with an average particle size of ca. 10 nm, which is close to the value calculated from the Rietveld refinement (10.9 nm). A very small amount of them are larger elongated nanoparticles. The HRTEM image and corresponding Fourier transform (FT) (inset) of the roundish nanoparticle (Figure 5b) illustrate that it is single crystalline with well-developed crystal planes, while the elongated nanoparticles (Figure 5c) keep the wurtzite *hcp* structure of ZnO but with a preferential growth direction of along [100]. Figure 6 shows the zero-loss (ZL) filtered image with a 15 eV energy slit and O, Al, and Zn elemental maps obtained from the O-*K*, Al-$L_{2,3}$, and Zn-$L_{2,3}$ edges, respectively. The image intensity scales linearly with the concentration of the element that is mapped. This indicates that Al distributed in the nanoparticles homogeneously. To doublecheck the doping level, EDX of the Al:ZnO nanoparticles with different initial Al concentrations was also investigated; the results are plotted in Figure 3. In general, the results are similar to, but slightly higher than, the ones from the Rietveld refinement. This is understandable because EDX results can only provide local information and may include surface adsorption and amorphous phase, whereas the Rietveld refinement gives a more average result and only considers the crystal domain part.

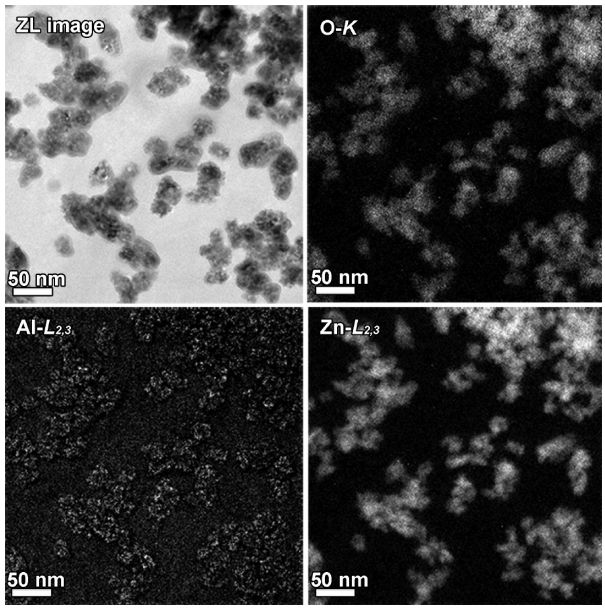

Figure 6. EFTEM elemental maps of $Al_{0.20}Zn_{0.80}O$ nanoparticles.

Band Gap. Figure 7a shows the optical reflection spectra of Al:ZnO powders with different initial Al concentrations. As ZnO is a direct band gap material, eqs 1 and 2 are used to calculate the energy band gap of these nanoparticles:[41,42]

$$2\alpha t = \ln\left(\frac{R_{max} - R_{min}}{R - R_{min}}\right) \quad (1)$$

$$\alpha h\nu = A(h\nu - E_g)^{1/2} \quad (2)$$

where α is the absorption coefficient, t is the thickness of the measured sample, and ν is the photon energy. According to the above relation, $(\alpha h\nu)^2$ versus $(h\nu)$ for Al:ZnO are plotted (Figure 7a, inset). Extrapolation of the linear part of the absorption edge leads to the axis interception, which corresponds to the band gap E_g. The band gap of all Al:ZnO samples are smaller than that of pure ZnO (3.26 eV). There is a small "blue shift", which changes from 3.06 to 3.10 eV with increasing the initial Al concentration from 5 to 20 mol % (Figure 7b). Similar results were reported for other doped ZnO samples.[23,43,44] This band gap narrowing effect is ascribed to the emerging of the dopant band formed by the overlapped dopant energy levels. The lack of Burstein–Moss effect[45] in our

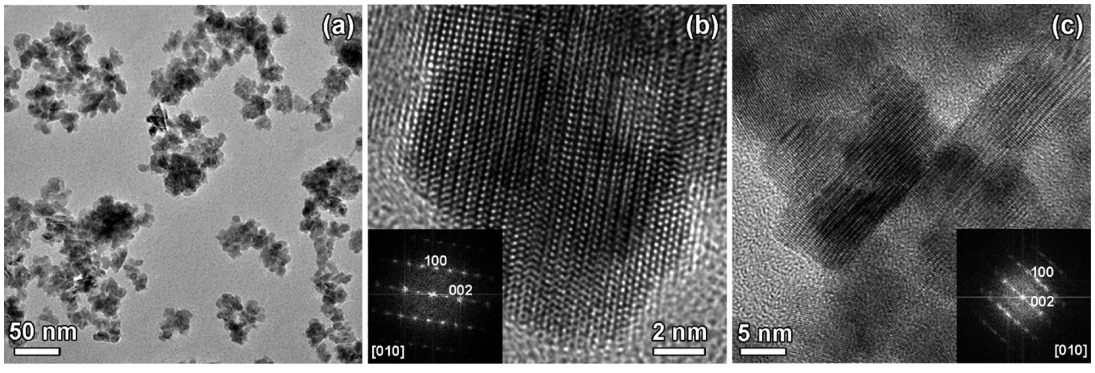

Figure 5. (a) TEM image of $Al_{0.20}Zn_{0.80}O$ nanoparticles, (b) HRTEM image of the roundish nanoparticles (inset = corresponding FT), and (c) HRTEM image of the elongated nanoparticles (inset = corresponding FT).

dx.doi.org/10.1021/sc300073d | *ACS Sustainable Chem. Eng.* 2013, 1, 152–160

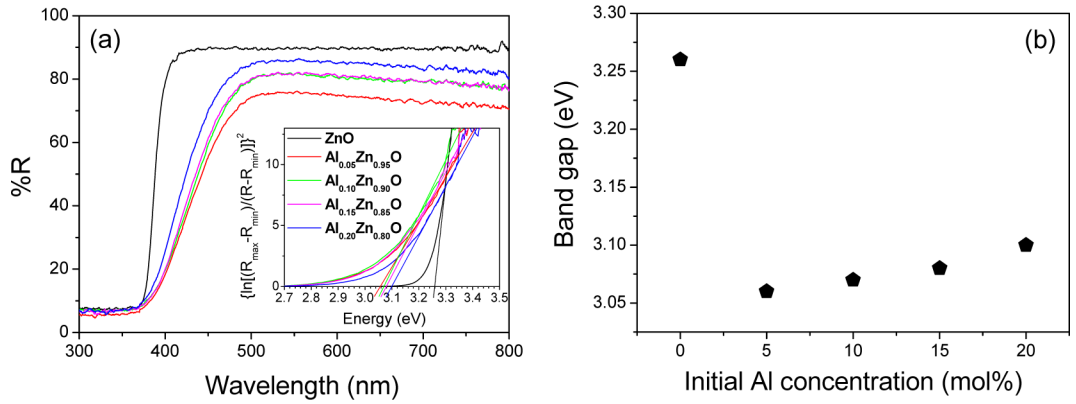

Figure 7. (a) Optical reflection spectra of $Al_nZn_{1-n}O$ powders with n = 0, 0.05, 0.10, 0.15, and 0.20 (inset = plots of $(\alpha h\nu)^2$ versus $(h\nu)$) and (b) calculated band gap versus different initial Al concentrations.

samples indicates that the Fermi level did not move into the conduction band after doping.

Thermal Analysis. To check the phase stability of Al:ZnO nanoparticles at elevated temperatures, HTXRD patterns were measured. The PXRD patterns of $Al_{0.10}Zn_{0.90}O$ nanoparticles at different temperatures are shown in Figure S1 (Supporting Information). The phase was stable up to 600 °C for 2 h. Only the crystallites slightly grew from 13 to 19 nm. Further increase of the temperature up to 800 °C resulted in crystallites of 50 nm, and a second phase of $ZnAl_2O_4$ (ICDD PDF no. 70-8182) appeared. The FT-IR spectrum (Supporting Information, Figure S2) of the as-synthesized powders shows strong absorption peaks at 1580, 1420, 1350, and 1050−1010 cm^{-1}, which can be ascribed to the aromatic C═C stretching, C═O stretching, C−H bending, and C−O bending vibration, respectively. All these peaks disappeared after the thermal treatment at 400 °C for 1 h, proving that all the organics are completely removed at this temperature. To avoid formation of side phases, the heat treatment of the films was carried out at 600 °C.

Al-Doped ZnO Thin Films. *Film-Deposition Process.* The film-deposition process is illustrated in Figure 8. The as-

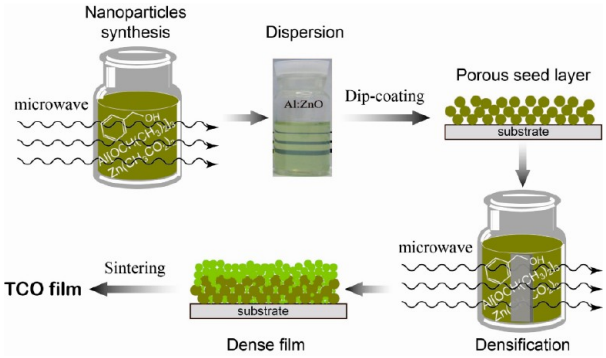

Figure 8. Schematic illustration of film-deposition process.

synthesized wet powders were dispersed in ethanol without any surfactants. Then a seed layer was deposited on fused silica substrate by dip-coating. Because only porous films can be obtained by this procedure, a densification step was applied to improve the microstructure of the film (for details, see Experimental Section). In this case, the seed layer with the substrate was immersed in the reaction solution, and the microwave-assisted reaction was repeated. As nucleation prefers to start on the surface of the particles, the pores are filled. In addition, a new layer was grown on the top of the seed layer. Hence, the density as well as the thickness of the film was increased. In the end, sintering at 600 °C for 2 h in air was applied to remove organics and improve the conductivity of the films. The densification step could be repeated several times to reach the required density and thickness. If the glass substrate is directly immersed in the reaction solution without a seed layer, then an inhomogeneous film consisting of isolated islands is formed. This is in contrast to previous results with ferrite and perovskite nanoparticle films, which directly grow homogenously on glass without a seed layer.[46]

Structure and Morphology of the Films. All of the Al:ZnO films with different doping levels were prepared under the same conditions, and the structure and morphology of those films were very similar. Taking $Al_{0.10}Zn_{0.90}O$ film as an example, Figure 9 shows the surface morphology and cross section of the sintered films with and without densification. It is obvious that all the films are homogeneous over a large area. Without densification, the film is quite porous. However, after applying

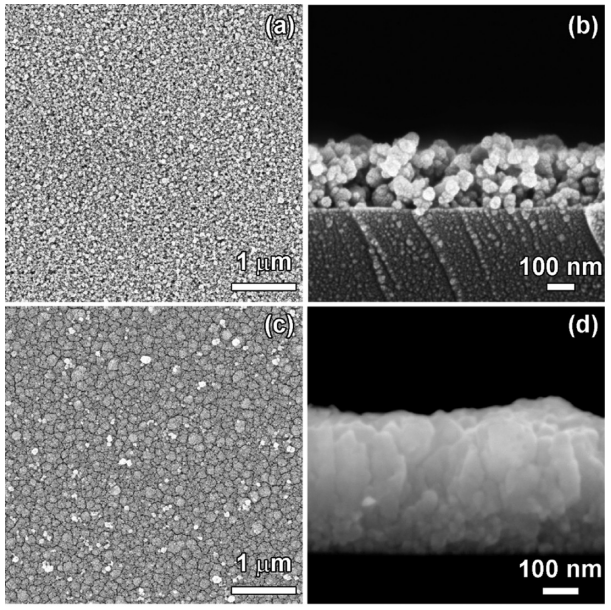

Figure 9. SEM images of the sintered $Al_{0.10}Zn_{0.90}O$ film: (a) the surface and (b) cross section of the film without densification; (c) the surface and (d) cross section of the film densified three times.

dx.doi.org/10.1021/sc300073d | ACS Sustainable Chem. Eng. 2013, 1, 152−160

three times the microwave-assisted reaction densification step, the film became relatively dense and the thickness doubled. After annealing, the structure of the cross section changed from a granular structure to a columnar structure as shown in Figure 9b and d. The columnar structure indicates a preferred growth direction during the densification and annealing step, which is in accordance with the XRD analysis shown in Figure 10. It reveals that the nanoparticles in the film were reoriented and grown along the [002] direction.

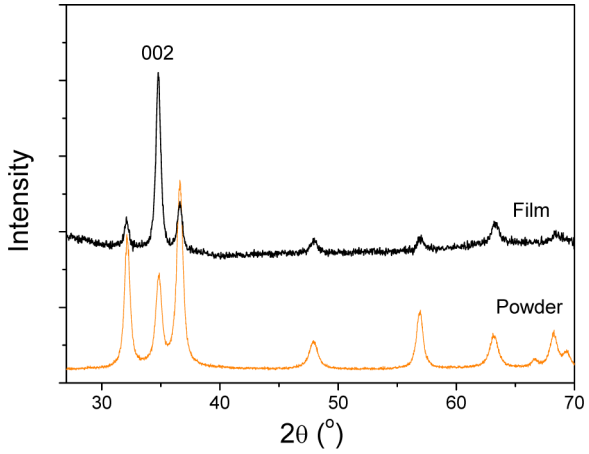

Figure 10. XRD patterns of $Al_{0.10}Zn_{0.90}O$ powder and densified film after annealing at 600 °C for 2 h.

Figure 11 shows the AFM image of the same $Al_{0.10}Zn_{0.90}O$ film as shown in Figure 9c. The film surface roughness shows a

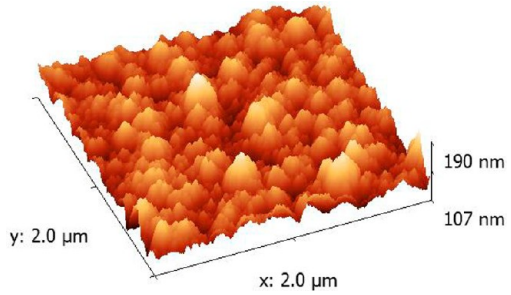

Figure 11. AFM image of the densified $Al_{0.10}Zn_{0.90}O$ film.

wavy variation, and the root-mean-square (Rms) roughness is about 10 nm. Depending on different applications, the requirement of surface roughness is different. For instance, the smoother the TCO surface, the better it is for light-emitting diodes; whereas as a top layer of the solar cells, wavy surfaces can reduce the reflection of light to improve the efficiency.

Electrical Properties of the Films. Figure 12 shows the dependence of the electrical properties of Al:ZnO films on the initial Al concentration. To investigate the influence of the Al concentration on the resistivity (ρ), the thicknesses of the films with different doping levels were kept as similar as possible. The corresponding thicknesses of the films are shown in Figure 12 as well. With increasing Al concentration, the resistivity first decreases and then increases. The minimum appears at the initial Al concentration of 10%. This observation could be well-explained with the Rietveld analysis of the X-ray data. Refinement of the atomic occupancy indicated that the doping level saturated around 8% (Figure 3). This might explain why

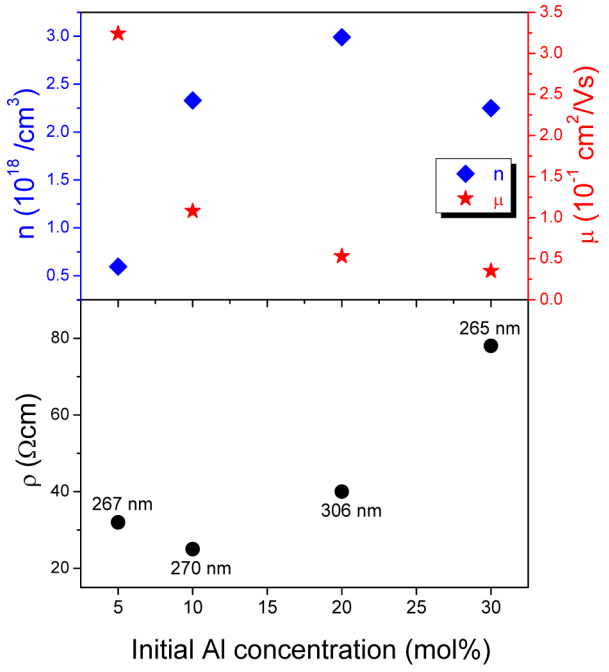

Figure 12. Dependence of the resistivity (ρ), mobility (μ), and carrier concentration (n) of Al:ZnO films (with different thicknesses of 267, 270, 306, and 265 nm) on the initial Al concentration.

the carrier concentration (n) increases with increasing the initial Al concentration up to 10% and keeps more or less the same above this concentration (Figure 12). Below that saturation it is true that the higher the doping level, the lower is the resistivity. When the saturation is reached, the average crystal size, derived from the Rietveld analysis, reduces with increasing the initial Al concentration (Figure 4). Therefore, the Hall mobility (μ) decreases, as shown in Figure 12, due to the stronger lattice scattering and grain boundary scattering effect, and this might explain why the resistivity becomes worse even though the doping level is approximately the same.

As the microstructure and thickness of the film have a strong influence on the electrical resistivity, the dependence of the resistivity on the densification step repetitions was investigated as well. Figure 13 shows the resistivity of $Al_{0.10}Zn_{0.90}O$ film as a function of the number of densification steps. The resistivity of

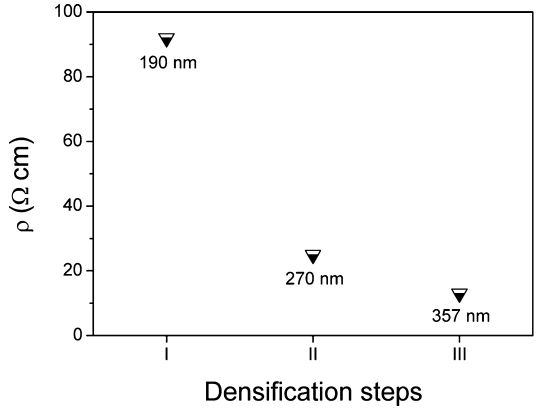

Figure 13. Dependence of the electrical resistivity of $Al_{0.10}Zn_{0.90}O$ films on the number of densification steps, which also results in increasing film thicknesses from 190 to 357 nm.

dx.doi.org/10.1021/sc300073d | ACS Sustainable Chem. Eng. 2013, 1, 152−160

the dip-coated film is too high to be measured by our method. After one time densification, the resistivity reduced to 92.11 Ω·cm. With a second densification step, the resistivity is about four times lower. It further reduced to 12.66 Ω·cm by a third densification step.

Besides doping and densification, the annealing atmosphere has also a great impact on the electrical properties. After postannealing at 600 °C for 1 h in N_2, the resistivity of the $Al_{0.10}Zn_{0.90}O$ film, for example, decreased from its initial 12.66 to 2.35×10^{-2} Ω·cm (the carrier concentration is 6.78×10^{19}/cm^3, and Hall mobility is 3.92 cm^2/(V s)) due to the contribution of oxygen vacancy. This resistivity is considerably higher than the values obtained from the vapor-phase deposited Al:ZnO films (as shown in Table 1), mainly due to the restricted connectivity of the particles. However, compared to the recently reported resistivity of Al:ZnO films obtained from nanoparticle solutions,[23] this value is 1 magnitude lower. Furthermore, this result is comparable to the recently published result on ITO films (2.6×10^{-2} Ω·cm), which is one of the lowest resistivity of ITO films obtained from nanoparticle solution processes.[47]

Optical Transmittance of the Film. Figure 14 shows the optical transmittance spectrum of the film with the lowest resistivity ($Al_{0.10}Zn_{0.90}O$ film with thickness of 357 nm). The transmittance in the visible light range (400−800 nm) is >76%, with an average of 91.4%. Especially the transmittance for green light reaches up to 95%. The inset in Figure 14 shows the photo of the film compared with a substrate and background. The color is from the interference effect between the top and bottom surfaces of the film, and it varies with the thickness of the film.

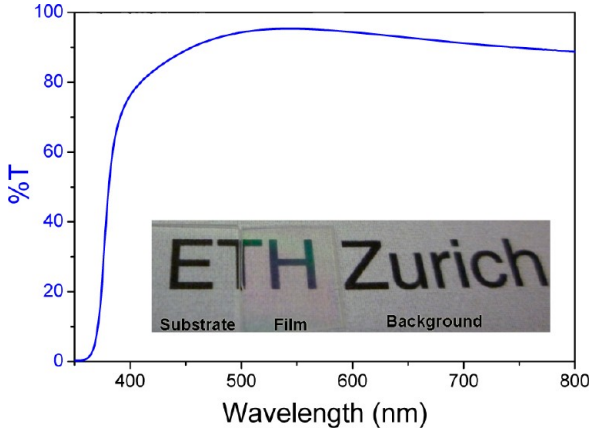

Figure 14. Optical transmittance spectrum of the film with the lowest resistivity ($Al_{0.10}Zn_{0.90}O$ film with thickness of 357 nm); inset = photo of the film compared with substrate and background.

Moisture Stability of Al:ZnO. The long-term performance reliability of TCO films is essential for any applications. One of the most important quality features is to be resistant to moisture. Therefore, the stability of Al:ZnO in a humid environment was investigated. Figure 15 shows the XRD patterns of $Al_nZn_{1-n}O$ (n = 0, 0.02, 0.05, 0.10, 0.20, and 0.30) nanoparticles in distilled water for 24 h at room temperature. A zinc aluminum carbonate hydroxide hydrate ($Zn_{0.71}Al_{0.29}(OH)_2(CO_3)_{0.145}\cdot xH_2O$) (ICDD PDF no. 48-1021) phase was formed for all doped samples, and the amount of this phase increased with increasing doping level. Figure 16 shows the SEM image of an $Al_{0.10}Zn_{0.90}O$ pellet surface. The surface layer was homogeneously transformed to the zinc aluminum carbonate hydroxide hydrate phase in a large area, and the morphology of this phase is platelet-like. Element maps also confirmed that the platelets are Al-rich and Zn-poor as shown in Figure 17. Cavani et al.[48] pointed out that, in nature, many compounds have been found that have the approximate composition of $M(II)_6M(III)_2(OH)_{16}CO_3\cdot 4H_2O$, indicating that it has a tendency to form $M(II)_{1-n}M(III)_n(OH)_2(CO_3)_{n/2}\cdot xH_2O$ when M(II) and M(III) ions, CO_3^{2-}, and H_2O exist. Therefore, a protective layer and/or sealing for Al:ZnO film is necessary for any applications under humid atmosphere. Work along this line is on progress in our research group.

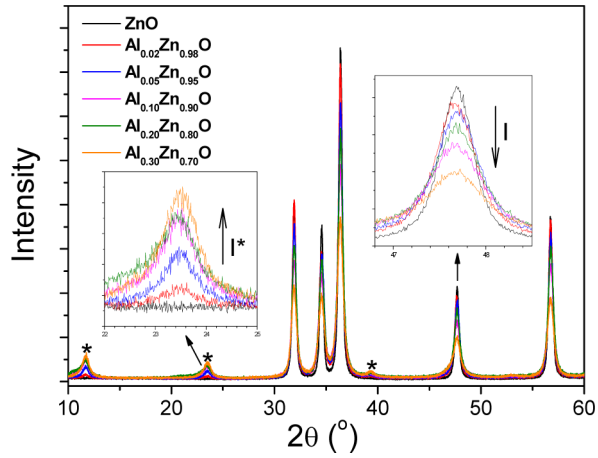

Figure 15. XRD pattern of $Al_nZn_{1-n}O$ nanoparticles after 24 h in distilled water at room temperature. Asterisk (*) indicates reflections from the $Zn_{0.71}Al_{0.29}(OH)_2(CO_3)_{0.145}\cdot xH_2O$ phase.

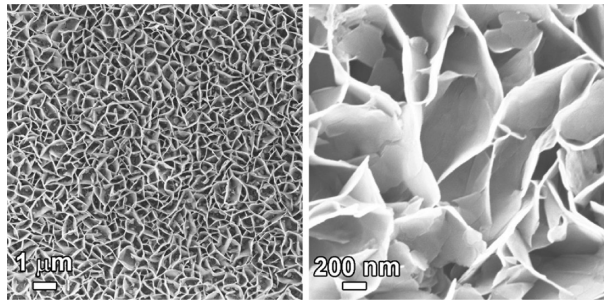

Figure 16. SEM image of $Al_{0.10}Zn_{0.90}O$ pellet surface after 24 h in distilled water at room temperature.

CONCLUSIONS

The microwave-assisted nonaqueous sol−gel process is a simple, economical, and time-efficient method that can be applied to the synthesis of Al:ZnO nanoparticles as building blocks for TCO films as well as to the densification of these films to increase the electrical conductivity. In addition, it is a powerful synthesis approach for the doping of such materials over a wide compositional range, which is important for the optimization of the properties. Although the characteristics of the nanoparticle building blocks such as doping level and crystal size explain the electrochemical properties of the films quite well, processing steps such as densification of the films and annealing under inert atmosphere are equally important. A minimum resistivity of 2.35×10^{-2} Ω·cm was obtained for a 357-nm-thick $Al_{0.10}Zn_{0.90}O$ film after postannealing under N_2,

dx.doi.org/10.1021/sc300073d | ACS Sustainable Chem. Eng. 2013, 1, 152−160

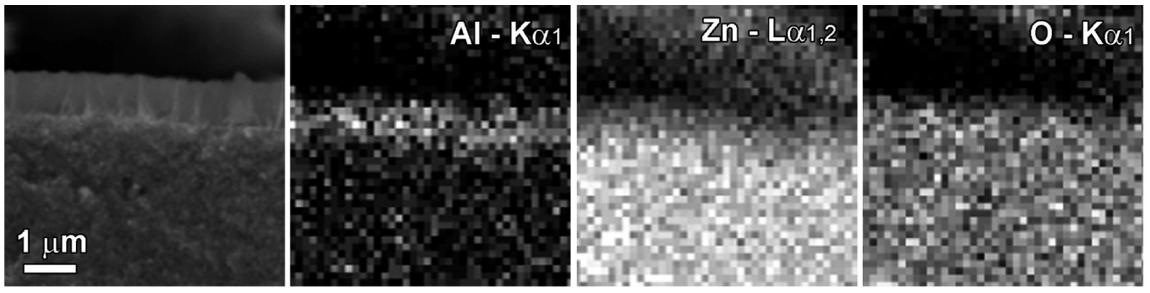

Figure 17. Secondary-electron SEM image and elemental maps of the cross section of $Al_{0.10}Zn_{0.90}O$ pellet after 24 h in distilled water at room temperature.

and the average transmittance in the visible light range was >90%. Although these results are promising on the way to the development of liquid-phase routes to TCO films, they also show that every step (synthesis of nanoparticles, preparation of dispersions, thin-film processing, and annealing) has to be optimized to produce TCO films of good quality.

■ ASSOCIATED CONTENT

Supporting Information

Powder X-ray diffraction patterns of $Al_{0.10}Zn_{0.90}O$ powders measured at different temperatures and FT-IR spectra of the as-synthesized and thermally treated $Al_{0.10}Zn_{0.90}O$ powders. This material is available free of charge via the Internet at http://pubs.acs.org.

■ AUTHOR INFORMATION

Corresponding Author

*E-mail: markus.niederberger@mat.ethz.ch.

Present Addresses

[‖]Electron Microscopy Center, EMPA, Swiss Federal Laboratories for Materials Science and Technology, Überlandstrasse 129, 8600 Dübendorf, Switzerland.

[⊥]Chevron Energy Technology Company, Chevron Way 100, Richmond, California 94801, United States.

Notes

The authors declare no competing financial interest.

■ ACKNOWLEDGMENTS

Financial support by ETH Zürich (ETH-0709-2) is gratefully acknowledged. We also thank Niklaus Kränzlin and Florian Heiligtag for fruitful discussions regarding the UV−vis and FT-IR spectra measurement and analyses.

■ REFERENCES

(1) Miyata, T.; Hikosaka, T.; Minami, T. High sensitivity chlorine gas sensors using multicomponent transparent conducting oxide thin films. *Sens. Actuators, B* **2000**, *69* (1−2), 16−21.

(2) Kiriakidis, G.; Suchea, M.; Dovinos, D. Transparent conducting oxides: From materials to sensing application. *Int. J. Offshore Polar Eng.* **2007**, *1−4*, 2942−2948.

(3) Mukherjee, N.; Ahmed, S. F.; Chattopadhyay, K. K.; Mondal, A. Role of solute and solvent on the deposition of ZnO thin films. *Electrochim. Acta* **2009**, *54* (16), 4015−4024.

(4) Chou, T. H.; Cheng, K. Y.; Hsieh, C. W.; Takaya, Y. Roll-to-roll fabrication of a low reflectance transparent conducting oxide film with subwavelength structures. *J. Micromech. Microeng.* **2012**, *22* (4), 045009.

(5) Brunnstrom, K.; Josefsson, K.; Andren, B. The effects of glossy screens on the acceptance of flat-panel displays. *J. Soc. Inf. Disp.* **2008**, *16* (10), 1041−1049.

(6) Tak, Y. H.; Kim, K. B.; Park, H. G.; Lee, K. H.; Lee, J. R. Criteria for ITO (indium-tin-oxide) an organic light thin film as the bottom electrode of emitting diode. *Thin Solid Films* **2002**, *411* (1), 12−16.

(7) Seo, J. W.; Oh, H. S.; Kwak, J. S. High efficiency vertical AlGaInP light emitting diodes with conductive omni-directional reflectors. *Curr. Appl. Phys.* **2011**, *11* (3), S385−S387.

(8) Tzeng, W. J.; Kao, C. C. Optimization of electro-luminescence performance of silicon quantum dots based light-emitting diode. In *INEC*; IEEE: New York, 2010; pp 1232−1233.

(9) Tun, C. J.; Sheu, J. K.; Pong, B. J.; Lee, M. L.; Lee, M. Y.; Hsieh, C. K.; Hu, C. C.; Chi, G. C. Applications of transparent Al-doped ZnO contact on GaN-based power LED. In *Gallium Nitride Materials and Devices*; Proc. of SPIE: Bellingham, WA, 2006; pp X1210−X1210.

(10) Ohta, H.; Kawamura, K.; Orita, M.; Sarukura, N.; Hirano, M.; Hosono, H. Room temperature operation of UV-LED composed of TCO hetero p-n junction, p-$SrCu_2O_2$/n-ZnO. In *MRS*; Cambridge University Press: Warrendale, PA, 2000; pp 283−288.

(11) Granqvist, C. G. Transparent conductors as solar energy materials: A panoramic review. *Sol. Energy Mater. Sol. Cells* **2007**, *91* (17), 1529−1598.

(12) Ahn, K. S.; Yoo, S. J.; Kang, M. S.; Lee, J. W.; Sung, Y. E. Tandem dye-sensitized solar cell-powered electrochromic devices for the photovoltaic-powered smart window. *J. Power Sources* **2007**, *168* (2), 533−536.

(13) Hauch, A.; Georg, A.; Baumgartner, S.; Krasovec, U. O.; Orel, B. New photoelectrochromic device. *Electrochim. Acta* **2001**, *46* (13−14), 2131−2136.

(14) Pattantyus-Abraham, A. G.; Kramer, I. J.; Barkhouse, A. R.; Wang, X. H.; Konstantatos, G.; Debnath, R.; Levina, L.; Raabe, I.; Nazeeruddin, M. K.; Gratzel, M.; Sargent, E. H. Depleted-heterojunction colloidal quantum dot solar cells. *ACS Nano* **2010**, *4* (6), 3374−3380.

(15) Sheel, D. W.; Yates, H. M.; Evans, P.; Dagkaldiran, U.; Gordijn, A.; Finger, F.; Remes, Z.; Vanecek, M. Atmospheric pressure chemical vapour deposition of F doped SnO_2 for optimum performance solar cells. *Thin Solid Films* **2009**, *517* (10), 3061−3065.

(16) Beneking, C.; Rech, B.; Wieder, S.; Kluth, O.; Wagner, H.; Frammelsberger, W.; Geyer, R.; Lechner, P.; Rubel, H.; Schade, H. Recent developments of silicon thin film solar cells on glass substrates. *Thin Solid Films* **1999**, *351* (1−2), 241−246.

(17) Ozgur, U.; Alivov, Y. I.; Liu, C.; Teke, A.; Reshchikov, M. A.; Dogan, S.; Avrutin, V.; Cho, S. J.; Morkoc, H. A comprehensive review of ZnO materials and devices. *J. Appl. Phys.* **2005**, *98* (4), 041201.

(18) Jin, Z. C.; Hamberg, I.; Granqvist, C. G.; Sernelius, B. E.; Berggren, K. F. Reactively sputtered ZnO-Al films for energy-efficient windows. *Thin Solid Films* **1988**, *164*, 381−386.

(19) Gong, L.; Ye, Z. Z.; Lu, J. G.; Zhu, L. P.; Huang, J. Y.; Gu, X. Q.; Zhao, B. H. Highly transparent conductive and near-infrared reflective ZnO:Al thin films. *Vacuum* **2010**, *84* (7), 947−952.

(20) Hu, J. H.; Gordon, R. G. Textured aluminum-doped zinc-oxide thin-films from atmospheric-pressure chemical-vapor deposition. *J. Appl. Phys.* **1992**, *71* (2), 880−890.

(21) Crossay, A.; Buecheler, S.; Kranz, L.; Perrenoud, J.; Fella, C. M.; Romanyuk, Y. E.; Tiwari, A. N. Spray-deposited Al-doped ZnO

transparent contacts for CdTe solar cells. *Sol. Energy Mater. Sol. Cells* **2012**, *101*, 283−288.
(22) Hilgendorff, M.; Spanhel, L.; Rothenhausler, C.; Muller, G. From ZnO colloids to nanocrystalline highly conductive films. *J. Electrochem. Soc.* **1998**, *145* (10), 3632−3637.
(23) Hammarberg, E.; Prodi-Schwab, A.; Feldmann, C. Microwave-assisted polyol synthesis of aluminium- and indium-doped ZnO nanocrystals. *J. Colloid Interface Sci.* **2009**, *334* (1), 29−36.
(24) Bilecka, I.; Djerdj, I.; Niederberger, M. One-minute synthesis of crystalline binary and ternary metal oxide nanoparticles. *Chem. Commun.* **2008**, *7*, 886−888.
(25) Bilecka, I.; Luo, L.; Djerdj, I.; Rossell, M. D.; Jagodic, M.; Jaglicic, Z.; Masubuchi, Y.; Kikkawa, S.; Niederberger, M. Microwave-assisted nonaqueous sol−gel chemistry for highly concentrated ZnO-based magnetic semiconductor nanocrystals. *J. Phys. Chem. C* **2011**, *115* (5), 1484−1495.
(26) Bilecka, I.; Niederberger, M. Microwave chemistry for inorganic nanomaterials synthesis. *Nanoscale* **2010**, *2* (8), 1358−1374.
(27) Luo, L.; Häfliger, K.; Xie, D.; Niederberger, M., Transparent conducting Sn:ZnO films deposited from nanoparticles. *J. Sol−Gel Sci. Technol.* **2012**, DOI: 10.1007/s10971-012-2709-7.
(28) Pasquarelli, R. M.; Ginley, D. S.; O'Hayre, R. Solution processing of transparent conductors: From flask to film. *Chem. Soc. Rev.* **2011**, *40*, 5406−5441.
(29) Coelho, A. A. TOPAS-Academic V4.1, http://www.topas-academic.net/.
(30) Young, R. A. *The Rietveld Method.*; IUCr/Oxford University Press: New York, 1993.
(31) Finger, L. W.; Cox, D. E.; Jephcoat, A. P. A correction for powder diffraction peak asymmetry due to axial divergence. *J. Appl. Crystallogr.* **1994**, *27*, 892−900.
(32) Dollase, W. A. Correction of intensities for preferred orientation in powder diffractometry—Application of the march model. *J. Appl. Crystallogr.* **1986**, *19*, 267−272.
(33) Snyder, R. L.; Bunge, H. J.; Fiala, J. *Defect and Microstructure Analysis by Diffraction*; IUCr/Oxford University Press: New York, 1999.
(34) McCusker, L. B.; Von Dreele, R. B.; Cox, D. E.; Louer, D.; Scardi, P. Rietveld refinement guidelines. *J. Appl. Crystallogr.* **1999**, *32*, 36−50.
(35) Pitschke, W.; Hermann, H.; Mattern, N. Microabsorption of scattered X-rays and its dependence on incidence angle in the nonsymmetric reflection case. *J. Appl. Crystallogr.* **1993**, *26*, 132−134.
(36) Karvaly, B.; Hevesi, I. Investigations on diffuse reflectance spectra of V_2O_5 powder. *Z. Naturforsch., A: Phys. Sci.* **1971**, *A26* (2), 245−249.
(37) Wendlandt, W. W.; Hecht, H. G., *Reflectance Spectroscopy*; Wiley Interscience: New York, 1966.
(38) Murphy, A. B. Band-gap determination from diffuse reflectance measurements of semiconductor films, and application to photoelectrochemical water-splitting. *Sol. Energy Mater. Sol. Cells* **2007**, *91* (14), 1326−1337.
(39) Shannon, R. D. Revised effective ionic-radii and systematic studies of interatomic distances in halides and chalcogenides. *Acta Crystallogr., Sect. A* **1976**, *32* (Sep 1), 751−767.
(40) Stroppa, D. G.; Montoro, L. A.; Beltran, A.; Conti, T. G.; da Silva, R. O.; Andres, J.; Longo, E.; Leite, E. R.; Ramirez, A. J. Unveiling the chemical and morphological features of Sb−SnO_2 nanocrystals by the combined use of high-resolution transmission electron microscopy and ab initio surface energy calculations. *J. Am. Chem. Soc.* **2009**, *131* (40), 14544−14548.
(41) Smith, R. A. *Semiconductors*, Second ed.; Cambridge University Press: Cambridge, U.K., 1978.
(42) Nowak, M.; Kauch, B.; Szperlich, P. Determination of energy band gap of nanocrystalline SbSI using diffuse reflectance spectroscopy. *Rev. Sci. Instrum.* **2009**, *80* (4), 046107.
(43) Yung, K. C.; Liem, H.; Choy, H. S. Enhanced redshift of the optical band gap in Sn-doped ZnO free standing films using the sol−gel method. *J. Phys. D: Appl. Phys.* **2009**, *42* (18), 185002.
(44) Benelmadjat, H.; Boudine, B.; Halimi, O.; Sebais, M. Fabrication and characterization of pure and Sn/Sb-doped ZnO thin films deposited by sol−gel method. *Opt. Laser Technol.* **2009**, *41* (5), 630−633.
(45) Sernelius, B. E.; Berggren, K. F.; Jin, Z. C.; Hamberg, I.; Granqvist, C. G. Band-gap tailoring of ZnO by means of heavy Al doping. *Phys. Rev. B* **1988**, *37* (17), 10244−10248.
(46) Kubli, M.; Luo, L.; Bilecka, I.; Niederberger, M. Microwave-assisted nonaqueous sol−gel deposition of different spinel ferrites and barium titanate perovskite thin films. *Chimia* **2010**, *64* (3), 170−172.
(47) Yarema, M.; Pichler, S.; Kriegner, D.; Stangl, J.; Yarema, O.; Kirchschlager, R.; Tollabimazraehno, S.; Humer, M.; Haringer, D.; Kohl, M.; Chen, G.; Heiss, W. From highly monodisperse indium and indium tin colloidal nanocrystals to self-assembled indium tin oxide nanoelectrodes. *ACS Nano* **2012**, *6* (5), 4113−4121.
(48) Cavani, F.; Trifiro, F.; Vaccari, A. Hydrotalcite-type anionic clays: Preparation, properties and applications. *Catal. Today* **1991**, *11* (2), 173−301.